OUTFLOWS AND HOT DUST EMISSION

1.1 INTRODUCTION

Reverberation measurements of nearby AGNs suggest that the near-infrared emission originates from very close to the central source (few tens of light days; e.g. Minezaki et al., 2004; Suganuma et al., 2006). The inferred temperature of the dust is high (T ~ 1200 K), and is close to the sublimation temperature of the dust grains (e.g. Barvainis, 1992). A natural interpretation is that the hot dust is at the innermost edge of the dusty torus, which is a key ingredient in unification schemes of AGN (Antonucci, 1993; Urry and Padovani, 1995). The dust reprocesses optical/ultraviolet photons from the accretion disc and re-emits in the near-infrared.

However, in recent years the picture has evolved away from a static 'doughnut' towards a more general circum-nuclear, geometrically and optically thick dust distribution. In the dusty wind model - first proposed by Konigl and Kartje, (1994) and later developed by, amongst others, Everett, (2005), Elitzur and Shlosman, (2006), Keating et al., (2012) - the torus is the dusty part of a magneto-hydrodynamic wind beyond the dust sublimation radius. Beyond some radius, this accretion disc is cool enough for dust accreting into it from the host interstellar medium not to be destroyed. Outflows may emerge from the outer region of the accretion disc, in which the gas clouds are dusty and relatively cold. The dusty clouds are uplifted above the disk where they are exposed to the central engine. The dust is heated by accretion disc photons, and radiates in the near-infrared band. The wind is roughly polar, and so the dust forms a vertical 'wall' around the accretion disc. This provides the circum-nuclear obscuration required by unification schemes. Recent results from mid-infrared interferometry, which find that the mid-infrared emission in nearby Seyfert galaxies is dominated by dust in the polar regions appear to support this picture (e.g. Hönig et al., 2013).

Since the physical processes that power AGN are generally understood only qualitatively, almost all AGN SED templates are empirical. The empirical template of Elvis et al., (1994) is

still the most commonly cited, despite many additions and updates (e.g. Polletta et al., 2000; Kuraszkiewicz et al., 2003; Risaliti and Elvis, 2004; Richards et al., 2006; Polletta et al., 2007; Lusso et al., 2010; Shang et al., 2011; Marchese et al., 2012; Trichas et al., 2012). However, these composite spectra are often constructed from quasars with a huge range in luminosity as a function of wavelength. In addition, the presence of significant host galaxy at optical wavelengths in low-redshift objects is an additional complication which has not always been taken care of adequately. There is therefore a strong rationale for taking a parametric approach to modelling quasar SEDs. This is the approach we take in this Chapter. We then investigate whether the systematic dependence of the model parameters on quasar properties including the BH mass, luminosity, accretion rate and outflow diagnostics.

The hot dust signature could contain information about inner face of an obscuring torus structure and/or constrain the dust content of an accretion disc wind. With large-scale surveys from SDSS, UKIDSS, and WISE providing information on the ultra-violet to infra-red SEDs of thousands of quasars at redshifts $2 \lesssim z \lesssim 3$, it is now possible to study the emission from hot (T $\sim$ 1200 K), parsec-scale dust in big samples with large dynamic range in luminosity and redshift. In recent years, many authors have investigated the hot dust properties of high redshift ($z \sim 2$) quasars. Found anti-correlations between the hot dust abundance and the torus covering factor (Roseboom et al., 2013), the quasar bolometric luminosity (Mor and Trakhtenbrot, 2011). However, need to be careful looking at trends with luminosity, as it means probing different parts of the SED. Gallagher et al., (2007) undertook a similar investigation for a much smaller sample of 234 radio-quiet quasars. Wang et al., (2013), fitting the near-infrared emission with a single power-law, found that objects with strong outflow signatures (blueshifted C IV) have more hot dust emission relative to the accretion disc emission in a large sample of $z \sim 2$ non-BAL quasars. At lower redshifts, Shen and Ho, (2014) have found that the hot dust properties are correlated with EV1. Several other investigations have drawn attention to the rest-frame near-infrared SEDs, with populations of 'dust free' objects postulated (Hao et al., 2010; Hao et al., 2011; Jiang et al., 2010; Mor and Trakhtenbrot, 2011).

We can link it to the detailed investigations we have done using the SDSS spectra. In this Chapter, we investigate the re-

Survey	Band	λ_{eff} [micron]	AB offset	$A_{\mathrm{filter}}/E(B-V)$
SDSS	u	0.3543	0.913	4.875
	g	0.4770	−0.081	3.793
	r	0.6231	0.169	2.721
	i	0.7625	0.383	2.099
	z	0.9134	0.542	1.537
UKIDSS	Y	1.0305	0.641	1.194
	J	1.2483	0.941	0.880
	H	1.6313	1.378	0.569
	K	2.2010	1.897	0.352
WISE	W1	3.4	2.691	0.182
	W2	4.6	3.331	0.130
	W3	12.0		
	W4	22.0		

Table 1.1: Available photometry, effective wavelength, Vega to AB magnitude offsets, conversion from $E(B-V)$ to extinction. Need W3/W4 offsets.

lationship between hot dust properties and BLR outflows in a large sample of high redshift quasars. We use the information built up in previous Chapters of this thesis. Our approach has two stages. First, we build a simple parametric SED model that is able to reproduce the median optical-infrared colours of tens of thousands of SDSS AGN at redshifts $0 \lesssim z \lesssim 4$ (Section XX). Second, we measure the near-infrared SED properties of individual quasars, to understand the diversity of hot dust properties in the population (XX). We analyse the dependence of hot dust properties on BH mass, luminosity, accretion rate, and the strength of outflows in the BLR.

1.2 DATA

1.2.1 *SDSS DR7*

We use the Seventh Data Release (DR7) of the SDSS spectroscopic quasar catalogue (Schneider et al., 2010), which includes 105 783 objects across $\sim 9,380\,\mathrm{deg}^2$. The SDSS obtained images in five broad optical band-passes: u, g, r, i and z (Table 1.1). We use BEST point-spread function magnitudes from the catalogue.

1.2.2 *UKIDSS Large Area Survey*

We use the tenth data release (DR10) of the UKIRT Infrared Deep Sky Survey (UKIDSS; Lawrence et al., 2007) Large Area Survey (ULAS) which has observed $\sim 3,200$ deg^2 in four near-infrared band-passes: Y, J, H and K. We use 'apermag3' magnitudes, which are aperture corrected magnitudes in a $2''$ diameter aperture.

1.2.3 *WISE All-WISE Survey*

The Wide-field Infrared Explorer (WISE; Wright et al., 2010) mapped the entire sky in four mid-IR bands: W1, W2, W3 and W4. The WISE AllWISE Data Release ('AllWISE') combines data from the nine-month cryogenic phase of the mission that led to the 'AllSky' data release with data from the NEOWISE program (Mainzer et al., 2011). We use the profile-fitting magnitudes ('w1mpro', 'w2mpro' etc.)

1.2.4 *Photometry*

The mean flux density $f_\lambda(P)$ in a bandpass defined by a throughput function $P(\lambda)$ is given by:

$$f_\lambda(P) = \frac{\int P(\lambda) f_\lambda(\lambda) \lambda d\lambda}{\int P(\lambda) \lambda d\lambda} \qquad (1.1)$$

where $f_\lambda(\lambda)$ is the flux density of the object. The associated zero-point is calculated by evaluating the same expression for a reference object. In the AB system (Oke and Gunn, 1983) this is a constant spectral flux density of 3631 Jy. In the Vega system this is the star Vega. Magnitude offsets to convert Vega-based magnitudes onto the AB system are given in Table 1.1. In calculating these offsets we assume that the magnitude of Vega is 0.026 in the Vega magnitude system.

Ask Paul: Although the SDSS asinh magnitude system is intended to be on the AB system, the photometric zero-points are known to be slightly off the AB standard. According to the documentation[1], the u band zero-point is in error by 0.04 mag ($u_{AB} = u_{SDSS} - 0.04$) while the z band is in error by 0.02 ($z_{AB} = z_{SDSS} + 0.02$). The g, r and i zero-points are consistent

---

1 http://classic.sdss.org/dr7/algorithms/fluxcal.html

1.2.5   *Galactic extinction correction*

$A(u)$, the Galactic extinction in the u band at the position of the object, is given in the SDSS catalogue. It is computed using the maps of Schlegel, Finkbeiner, and Davis, (1998). We divide by 5.155 to get $E(B - V)$, the relative extinction between the B and V bands. Conversions from the selective extinction $E(B - V)$ to the total extinction $A(\lambda)$ in each band-pass were calculated according to equation B2 in Schlegel, Finkbeiner, and Davis, (1998) using a quasar SED template. These are given in the table. Do we also assume an extinction curve?

1.2.6   *Cross-matching*

There are 105 783 objects in the SDSS DR7 quasar catalogue. Cross-matching this catalogue to the UKIDSS (with a $2''$ matching radius) and WISE (with a $3''$ matching radius) catalogue leaves 36 607 objects. The UKIDSS footprint is only a fraction of the SDSS footprint, which is the reason a large fraction of objects could not be matched to UKIDSS.

We include only the 20 637 quasars with i band magnitudes brighter than 19.1, i.e. the quasars selected by the main SDSS quasar selection algorithm for quasars with colours consistent with being at redshifts $z < 3$ (Richards et al., 2002). For a given i magnitude, a quasar with a blue spectrum is more likely to be undetected at longer wavelengths than a quasar with a red spectrum. Therefore, as we allow fainter quasars into our sample we will be biased towards objects with redder spectra. We verified that above the $i = 19.1$ limit the sample is 95 per cent complete in all band-passes (excluding WISE $W3$ and $W4$).

Broad absorption line (BAL) quasars typically have redder spectra than non-BAL quasars. We therefore exclude these objects from our sample using the catalogue of BALs generated by Allen et al., (2011).

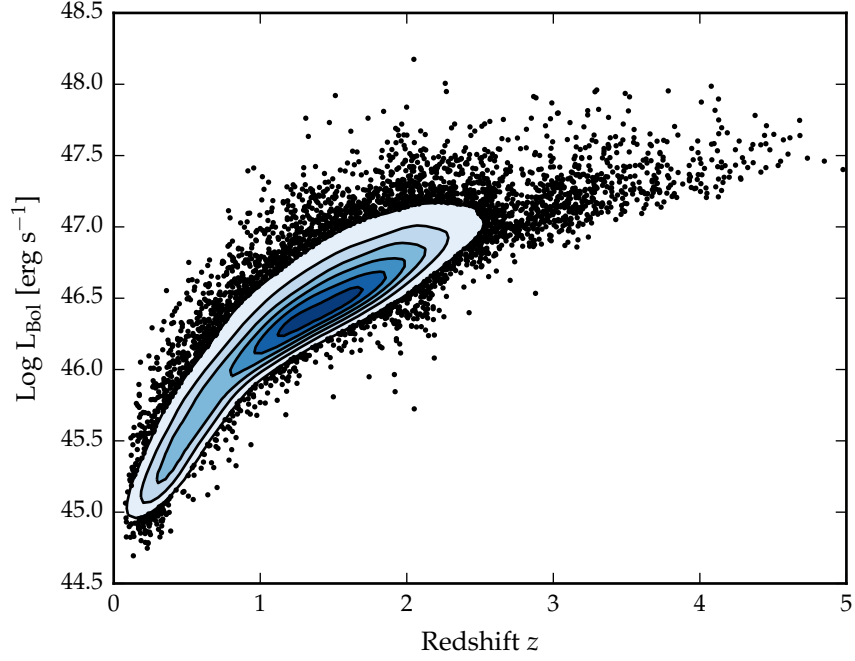The redshift and luminosity distribution of the final sample, containing 19,837 quasars, is shown in Figure 1.1.

Figure 1.1: Distribution of our sample in the redshift-luminosity plane. Remake with new sample

1.2.7 *Generating the quasar catalogue*

1.3 QUASAR SED

We have 19 853 quasars with photometric data from SDSS, UKIDSS and WISE. Our quasars cover the redshift range $0.2 < z < 4$, and so this data covers the rest-frame wavelength range from 800 Å to 3.8 micron. In this region the SED is dominated by the accretion disc, emission-lines and thermal emission from the hottest (T ~ 1200K) dust. Host galaxy emission is also significant for quasars at redshifts $z \lesssim 1$, and the effect of dust extinction at the AGN redshift is another factor which must be considered. In this Section, we describe how we have modelled emission from these different physical processes. At high redshifts, absorption due to Ly-α forest absorption becomes significant. Because we do not attempt to model this effect, our model is valid only at wavelengths long-ward of 1216 Å. We model dust emission using a single temperature (T ~ 1200 K) blackbody, which peaks at ~ 2 micron. At longer wavelengths, emission from cooler dust at greater radii from the central engine becomes increasingly important. We do not include this emission in our model, which restricts its validity to $\lesssim$ 3 mi-
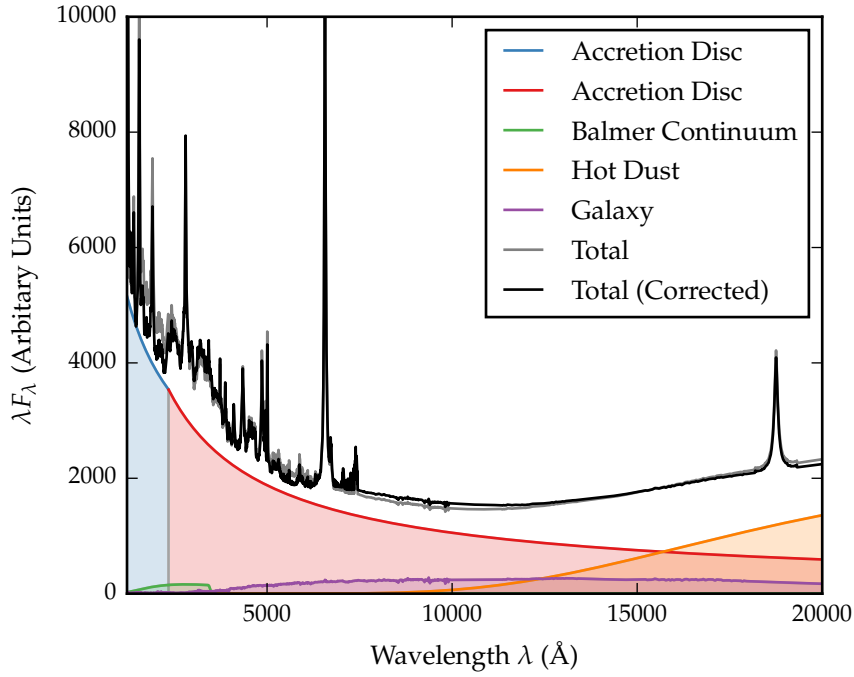
Figure 1.2: Model quasar spectrum at $z = 1$, showing the contributions to the total flux from the blue power-law slope, red power-law slope, Balmer continuum, blackbody, emission-line spectrum and host galaxy. Make sure it is immediately clear in every caption what is being shown in the figure.

cron. The model spectrum is shown in Figure 1.2, with each of the main components indicated.

1.4 SED MODEL

1.4.1 *Accretion Disc*

Thermal accretion disc emission in the $0.1 - 1$ micron region is characterised by a broken power-law with three free parameters: a break-wavelength λ_{break}, a blue power-law index α_{blue} for wavelengths shorter than the break wavelength, and a red power-law index α_{red} for wavelengths longer than the break wavelength.

1.4.2 *Balmer Continuum*

High order Balmer lines, optically thin Balmer continuum emission, two-photon emission and Fe II emission blend together to form a distinct feature in quasar spectra at $\sim 3000\text{Å}$. This is referred to as the 'Balmer' continuum. We simulate the Balmer continuum we use the empirical model given by Grandi, (1982):

$$F(\lambda) = C_{BC} \times B_\lambda(T_e)(1 - e^{-\tau_\lambda}); \quad \lambda \leqslant \lambda_{BE} \tag{1.2}$$

where C_{BC} is a normalisation factor, $B_\lambda(T_e)$ is the Planck function, $T_e = 13150\text{K}$ is the effective temperature, $\lambda_{BE} = 3460\text{Å}$ is the wavelength at the Balmer edge, and $\tau_\lambda = \tau_{BE}\left(\lambda_{BE}/\lambda\right)^{-3}$ is the optical depth with $\tau_{BE} = 45$ the optical depth at λ_{BE}. This function is convolved with a Gaussian with $\sigma = 5000\text{km s}^{-1}$ to simulate the effect of bulk velocity shifts comparable to those present in broad AGN emission-lines.

1.4.3 *Hot Dust*

Thermal emission from hot dust, which dominates the SED at wavelengths longer than 1 micron, is modeled using a blackbody

$$F_\lambda = C_{BB} \times \frac{2hc^2}{\lambda^5}\frac{1}{e^{\frac{hc}{\lambda k_B T_{BB}}} - 1}, \tag{1.3}$$

with two free parameters: the temperature T_{BB} and normalisation C_{BB} relative to the power-law continuum.

1.4.4 *Emission Lines*

We use an emission-line template taken from Francis et al., (1991), which has been extended by Maddox and Hewett, (2006) to include the Hα and Paα emission-lines[2]. All emission-lines, with the exception of Hα and Hβ , are scaled using a single free parameter C_{EL}, which preserves relative EQWs:

$$F_\lambda = C_{EL} \times \frac{F_{\lambda,el}}{F_{\lambda,cont}} \times F_\lambda \tag{1.4}$$

---

2 The spectrum is not significantly different from the Vanden Berk et al., (2001) SDSS composite

where $F_{\lambda,el}$ is the emission-line template, $F_{\lambda,cont}$ is the continuum flux in the template, and F_λ is the continuum flux in the SED model. Hα and Hβ are scaled separately:

$$F_\lambda = C_{EL} \times C_{H\alpha} \times \left(\frac{L(z)}{L(z_{nrm})}\right)^{-\beta} \times \frac{F_{\lambda,el}}{F_{\lambda,cont}} \times F_\lambda \qquad (1.5)$$

The luminosity dependence of the Hα EQW (i.e. the Baldwin effect) is parametrised with a power-law with slope $\beta = 0.04$. The redshift dependence of the mean AGN luminosity $L(z)$ for the SDSS quasar catalogue has been determined empirically.

1.4.5 *Host Galaxy*

Emission from the host galaxy is important for AGN at redshifts $z \lesssim 1$, particularly in the region around the 1 micron inflection point in the quasar SED. We use a $z = 0$ Sb template from Mannucci et al., (2001), which does not evolve with redshift. The template is scaled by a multiplicative factor C_{Gal} and added to the AGN SED. We define a new parameter, η, the fractional contribution from the host galaxy to the total flux in the interval 4000 and 5000 Å:

$$\eta \equiv \frac{C_{Gal}F_{Gal}}{F_{AGN} + C_{Gal}F_{Gal}}, \qquad (1.6)$$

where F_{Gal} and F_{AGN} are the flux of the galaxy and AGN respectively. Rearranging for the scaling factor C_{Gal} gives:

$$C_{Gal} = \frac{\eta}{1 - \eta} \frac{F_{AGN}}{F_{Gal}}. \qquad (1.7)$$

The fractional contribution to the total emission from the host galaxy decreases as the AGN luminosity increases and, in a flux-limited sample, the mean AGN luminosity increases as the redshift increases. Therefore, the size of the host galaxy contribution to the SED is diminished for AGN at high redshifts ($z \gtrsim 1$). At the same time, the shapes of the AGN and galaxy SEDs are very different. The galaxy SED peaks at ~ 1 micron, and falls away towards shorter wavelengths. On the other hand, the AGN SED continues to increase short-ward of 1 micron. Therefore, the contrast between the AGN and galaxy luminosity increases as the redshift increases. We parametrize the

AGN luminosity dependence of the host galaxy luminosity as a power-law:

$$\frac{L_{Gal}}{L_{AGN}} = L_{AGN}^{\beta-1} \tag{1.8}$$

with slope $\beta = 0.42$ (Croom et al., 2004). The galaxy scaling factor C_{Gal} becomes

$$C_{Gal} = \frac{\eta}{1-\eta} \frac{F_{AGN}}{F_{Gal}} \left[\frac{L_{Gal}(z)}{L_{AGN}(z)}\right] \left[\frac{L_{Gal}(z_{nrm})}{L_{AGN}(z_{nrm})}\right]^{-1} \tag{1.9}$$

$$= \frac{\eta}{1-\eta} \frac{F_{AGN}}{F_{Gal}} \left[\frac{L_{AGN(z)}}{L_{AGN(z_{nrm})}}\right]^{\beta-1}, \tag{1.10}$$

where z_{nrm} is an arbitrary redshift at which the fractional contribution from the host galaxy is by definition η.

1.4.6 *Dust Extinction*

The selection criteria of the SDSS DR7 quasar catalogue are sensitive to quasars with moderate amounts of dust reddening at the redshift of the quasar, and so we included the effect of dust extinction in our model. We use an extinction curve appropriate for the quasar population which has been derived by Paul Hewett. To derive the quasar extinction curve, UKIDSS photometry was used to provide an $E(B-V)$[3] estimate, via the magnitude displacement of each quasar from the locus of un-reddened objects. At redshifts $2 < z < 3$ the reddening measure is made at rest-frame wavelengths $3500 - 7000$ Å, where Galaxy, LMC and SMC extinction curves are very similar. The SDSS spectra of the same objects are then employed to generate an empirical extinction curve in the ultraviolet, down to 1200 Å. The resulting curve has no 2200 Å feature and rises rapidly with decreasing wavelength but is not as steep as the SMC curve. The extinctions curves give the colour excess $E(B-\lambda) = A$ relative to the colour excess $E(B-V)$ as a function of wavelength λ. The colour excess $E(B-V)$ is related to the extinction in the V band, $A(V)$, via the ratio R:

$$R_V = \frac{A(V)}{E(B-V)} \tag{1.11}$$

---

3 $E(B-V) = A(B) - A(V)$

where we assume $R_V = 3$. Hence the extinction at a wavelength lambda $A(\lambda)$ is

$$A(\lambda) = E(B - V) \times \left[\frac{E(\lambda - V)}{E(B - V)} + R \right] \qquad (1.12)$$

where the colour excess $E(B - V)$ is a free parameter in our model. The attenuation of the flux at a given wavelength is then:

$$F_\lambda = F_\lambda 10^{-A(\lambda)/2.5} \qquad (1.13)$$

in the rest frame of the quasar.

1.4.7 *Empirical Correction*

Describe Paul's empirical correction.

1.5 THE 'STANDARD' SED MODEL

- Given the same parameters, my model and Paul's look identical

- I'm generating model colours using my model and Paul's best-fit parameters, and Paul's correction

- Do my model colours look the same as Paul's? (i.e. is there a bug in my code?)

- Can I generate the same median colours as Paul? (i.e. what sample is being used? what magnitudes?)

- Can I do my own fit to the data?

We will begin by fitting a single SED model to all $19\,853$ quasars, encompassing a range of redshifts, luminosities, accretion rates etc. The free parameters in our model are summarised in Table 1.2. The reddening $E(B - V)$ is fixed to zero, since a large fraction of SDSS quasars have very small amounts of dust reddening (Richards et al., 2003). We generate a set of model observed spectra at redshifts from $z = 0.25$ to $z = 3.75$
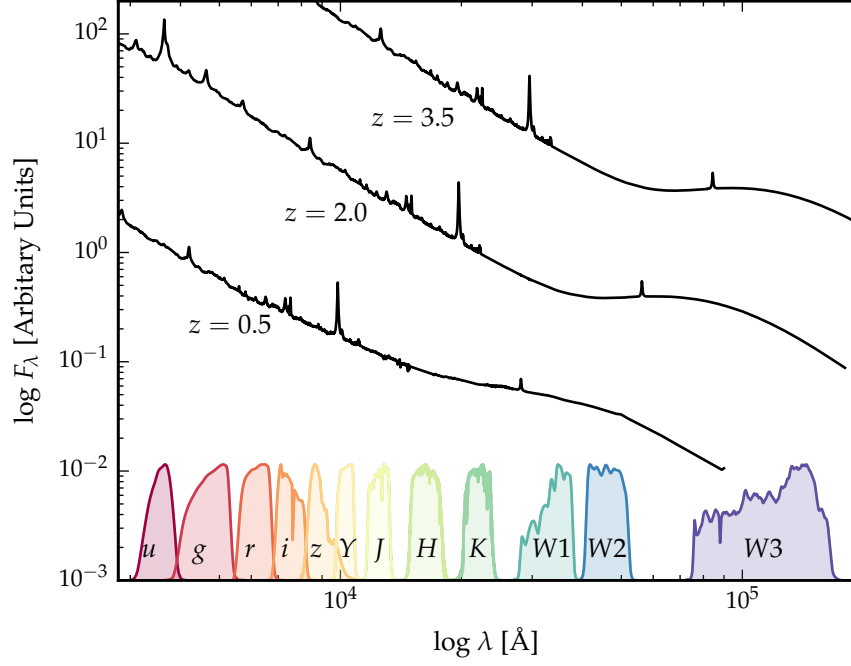
Figure 1.3: Model quasar spectrum at three different redshifts (each arbitrarily scaled), and throughput functions for SDSS, UKIDSS and WISE band-passes.

in intervals of $\Delta z = 0.1$. The SED model is shown at three different redshifts in Figure 1.3. The predicted broadband magnitude of the model is given by integrating the spectrum over the throughput for each of the bands.

$$m_\lambda(P) = -2.5\log(f_\lambda(P)) - m_0(P), \tag{1.14}$$

where $m_0(P)$ is the zero-point magnitude of band P and the mean flux density $f_\lambda(P)$ is given by

$$f_\lambda(P) = \frac{\int P(\lambda) f_\lambda(\lambda) \lambda d\lambda}{\int P(\lambda) \lambda d\lambda} \tag{1.15}$$

where $P(\lambda)$ is the dimensionless throughput function of the band-pass. Magnitudes are calculated in the AB system (Oke and Gunn, 1983), in which case the zero-point flux per unit wavelength is

$$\frac{f_\lambda(\lambda)}{\mathrm{erg\ cm^{-2}\ s^{-1} \mathring{A}^{-1}}} = 0.1087 \left(\frac{\lambda}{\mathring{A}}\right)^{-2}. \tag{1.16}$$

Parameter	Symbol	Value
Blue power-law index	α_{blue}	0.58
Red power-law index	α_{red}	−0.04
Power-law break	λ_{break}	2945
Blackbody temperature	T_{BB}	1216 K
Blackbody normalisation	C_{BB}	0.22
Emission-line scaling	C_{EL}	0.63
Hα emission-line scaling	$C_{H\alpha}$	0.63
Galaxy fraction	η	0.29

Table 1.2: Model parameters.

We divide our quasar sample into the same redshift bins. In each bin we normalise the quasar SEDs in the SDSS i band, and then calculate the median SED. The model SED in each redshift bin is similarly normalised. The chi-squared statistic is then minimised using the 'nelder-mead' algorithm (reference).

Our SED model is valid only up to $\lambda \sim 3$ micron in the quasar rest frame (the approximate wavelength of the peak in hot dust emission); beyond this additional contributions to the total flux from cooler dust will become significant. This prevents us from using the two longest wavelength WISE bands in the fit. We also exclude the SDSS u and g band-passes from the fit at $z > 2.7$ and $z > 3.7$ respectively, where these bands start to be affected by Lyα forest absorption.

1.6 RESULTS

The best-fitting parameters from the fit are shown in Table 1.2. The colours ($u - g$, $g - r$, etc.) of the median SED, the individual quasars, and the best-fitting model are plotted as a function of redshift in Figs. 1.4 and 1.5. Most of the large variations that can be seen in the median colours of the quasars as a function of redshift are due to strong emission-lines being redshifted into and out of the band-passes. Take away message is that a single, fairly simple parametric is able to reproduce the median colours of tens of thousands of AGN with a large dynamic range in redshift and luminosity. However, there is a significant scatter about the median model, which we will investigate in the next Section? Does any part of this scatter have a systematic dependence on properties of the BH (mass, accretion rate) or outflow diagnostics.

Re-do fit

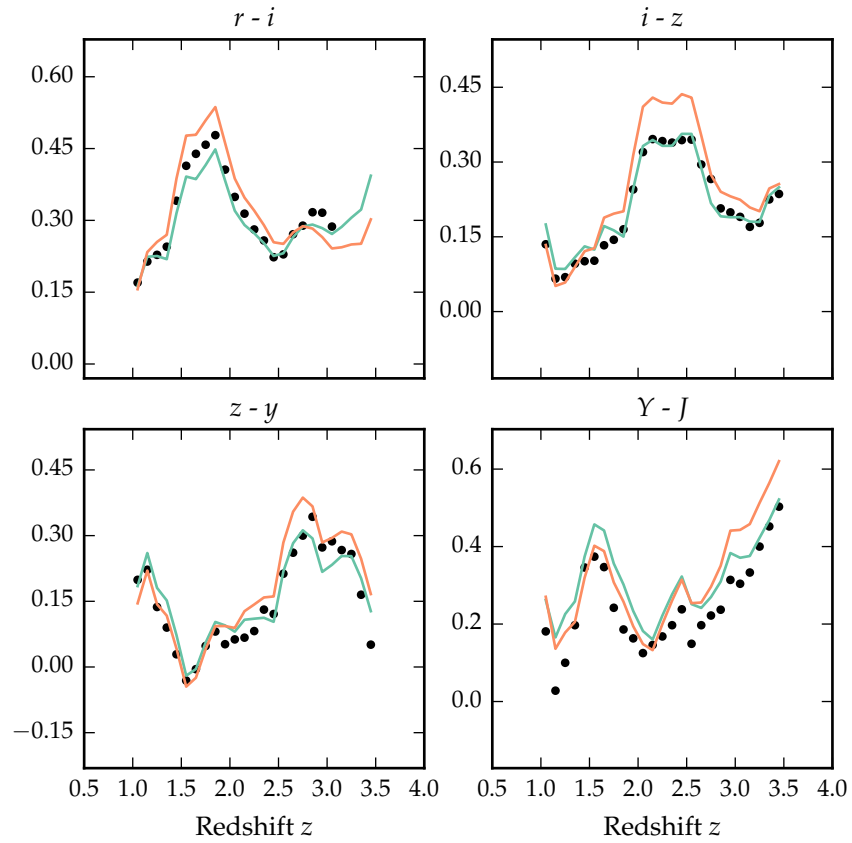*Need to show individual quasars.*

Figure 1.4: Colours of median quasar SED and best-fitting model, with and without correction. Corrected is in orange, uncorrected in green. Check with Paul. Correction often makes colours a lot worse. Once got to the bottom of this just show with correction. Is Lyman forest absorption / Lyman limit important for the quasars shown here.
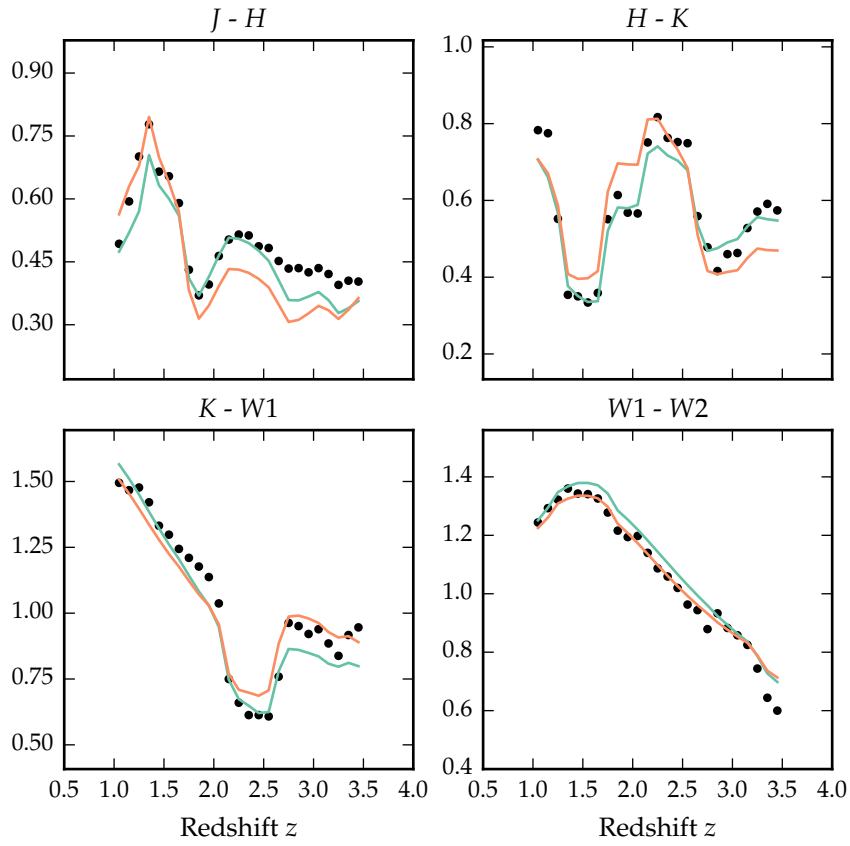
Figure 1.5: Colours of median quasar SED (*black circles*), individual objects (*grey points*), best-fitting model (*black line*) as a function of redshift.
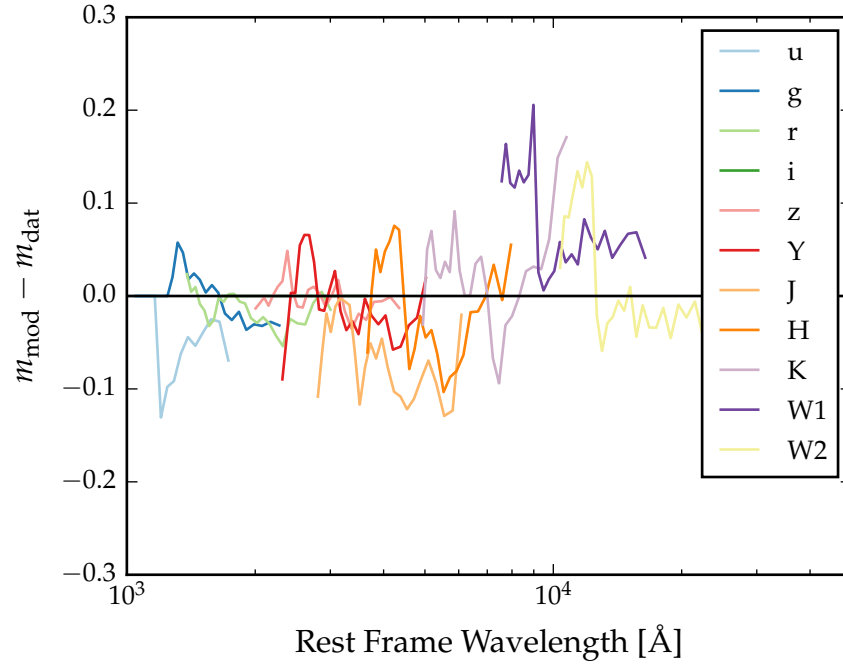
Figure 1.6: Residuals from fit as a function of rest-frame wavelength.
Need more info in caption.

1.7 DISCUSSION OF FIT

In Figure 1.6 we show the difference between the magnitudes
from the best-fitting model and the median magnitudes from
the sample. We have transformed the effective wavelengths of
the band-passes to the rest frame of the quasars in each redshift
bin, to give the residuals as a function of rest-frame wavelength.
We represent the residuals measured in each band-pass using
a different coloured line. Differences between residuals from
different band-passes at the same rest-frame wavelength could
indicate redshift evolution of the typical quasar SED.

The residuals indicate that over a large redshift range the
model does a fairly good at reproducing the median observed
colours of the sample. Most discrepancies are at the $< 0.1\,\mathrm{mag}$
level. A single model is effective at reproducing the median
colours, suggesting that the properties of a typical quasar do
not change significantly over a wide range of redshifts and lu-
minosities. One needs to take care in looking at trends with lu-
minosity given the observed-frame band-pass information on
the rest-frame SED can produce some strong systematics with
redshift, particularly if the SED-model is not a good fit to the
actual SED.

No: be quantitative
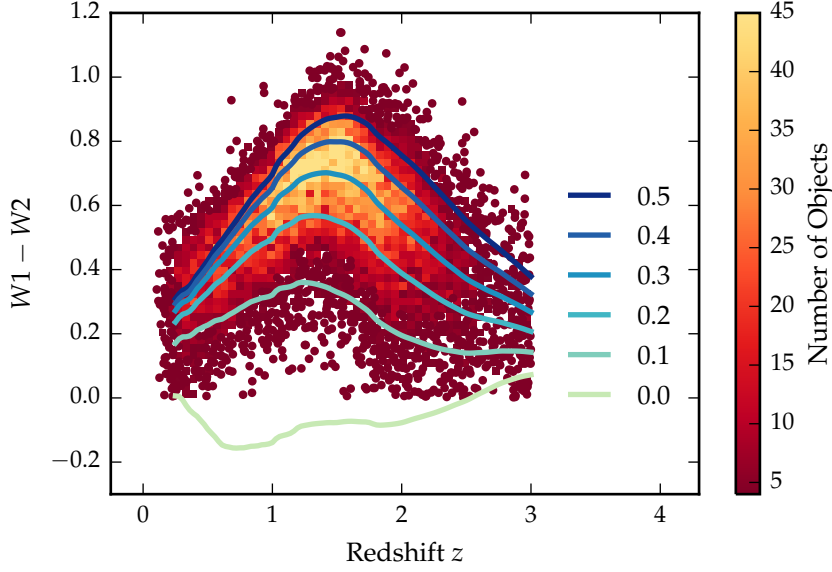
*Make sure this is
emphasised as a
new result.*

Figure 1.7: $W1 - W2$ colours of sample as a function of redshift. Above a certain density threshold points are represented by a density plot. On top we plot the colours of our standard SED model, with a fixed temperature and a varying near-infrared ($1 - 3$ micron) to ultra-violet ratio.

1.8 HOT DUST

The spread in the $W1W2$ colours (Figure 1.7), probing the rest-frame $\sim 1 - 2$ micron region, is significant and strongly suggests the presence of real variation in the hot dust temperature and luminosity among the quasars.

1.8.1 *Parametrising the hot dust emission*

We characterise the hot dust properties of our sample in terms of the temperature and luminosity of a blackbody. We choose to parametrise the luminosity in terms of the near-infrared to ultra-violet luminosity ratio. The ultra-violet and near-infrared luminosity are calculated between 2000 and 9000 Å and 1 and 3 micron respectively. This is roughly proportional to the covering factor of hot dust (L_{NIR}/L_{Bol}) used in some other studies (e.g. Roseboom et al., 2013). The temperature may be related to the distance of the dust from the central engine. The value of (L_{NIR}/L_{Bol}) is related to the covering factor of the hot dust.

Some previous studies (e.g. Wang et al., 2013; Zhang et al., 2014) have instead parametrised the near-infrared emis-

sion using a power-law ($\propto \lambda^{\beta_{NIR}}$), with $\beta \simeq 0.5$. We tested this parametrisation, and evaluated it's effectiveness relative to using a blackbody. We normalise the power-law at 9000 Å, where its flux is set equal to the flux of the ultra-violet/optical model. The near-infrared power-law slope is fit between ~ 1 and 2.4 micron (with the exact wavelength region being fit depending on the redshift of the quasar). We found large residuals in the best-fitting model which varied systematically as a function of $\lambda_{eff}/(1+z)$. This suggests that the blackbody is a better fit to the shape of the near-infrared emission than the power-law model (e.g. Gallagher et al., 2007).

1.8.2 *Sample*

Our goal is to determine the temperature and abundance of the hot dust component in individual quasars. These properties will be measured by fitting a model to the SDSS-UKIDSS-WISE photometry. Constraining a T $\sim$ 1200 K blackbody component in the SED model requires photometric data covering $\sim 1 - 3$ micron in the rest-frame of the quasar.

The observed-frame wavelength coverage of the available band-pass limits the redshift range of the quasars which can be used. We consider only quasars at redshifts $z > 1$ where the relative host galaxy contribution to the SED is negligible. At redshifts $1 \lesssim z \lesssim 1.5$ the available *ugrizYJHKW1W2* photometry provides good coverage of the rest-frame SED up to ~ 2 micron. At $z \sim 1.5$ the *W2* band-pass is shifted to ~ 1.8 micron; at higher redshifts *W2* is probing much shorter wavelengths than the peak of a T $\sim$ 1200 K blackbody. Because the shape of the blackbody is not well constrained by the available photometry, the uncertainty on the blackbody temperature measurement increases sharply for quasars at redshifts $z \gtrsim 1.5$

For the quasars at $z \sim 1$, the WISE *W3* band is probing rest-frame wavelengths of $\sim 5 - 6$ micron. This region of the SED is dominated by emission from cooler, more distant dust, which is not accounted for in our model. However, at redshifts $z \gtrsim 2$ the WISE *W3* band-pass probes sufficiently short wavelengths to be useful in constraining the shape of the hot blackbody component. Therefore, for quasars at redshifts $z > 2$ we again have sufficient constraints from the *ugrizYJHKW1W2W3* photometry to determine the temperature and normalisation of the blackbody component. There are few objects in our sample with redshifts $z > 2.7$, because the SDSS DR7 quasar selection algorithm

Sub-sample	Number of AGN	Data	Redshift range
Low-z	5,910	ugrizYJHKW1W2	$1 < z < 1.5$
High-z	1,989	ugrizYJHKW1W2W3	$2 < z < 2.7$

Table 1.3: Summary of sub-samples.

is highly incomplete at these redshifts. Therefore we set $z = 2.7$ as the upper limit on the redshift of our sample. Because of these constraints, our sample is divided into two parts: one at low redshifts ($1 < z < 1.5$) and the other at higher redshifts ($2 < z < 2.7$).

We impose a lower-limit signal-to-noise ratio S/N > 5 magnitudes in the K, $W1$ and $W2$ band-passes for the low-z sample and S/N > 5 in the $W1$, $W2$, and $W3$ band-passes for the high-z sample to ensure reliable photometry. This gives us 5 910 quasars in our low-z sample and 1 989 quasars in our high-z sample.

We will hold most model parameters fixed, and vary only the blackbody parameters which parametrise the near-infrared emission. Therefore, we need to define a sub-sample of objects which we know are well fit by our standard SED model in the ultra-violet/optical region. This means excluding objects with extreme emission-line EQWs and/or significant dust extinction. We use the $i - K$ colours of the quasars as a measure of the overall colour of the quasars as it provides the longest baseline in wavelength without being affected by absorption in the Lyα forest at high redshifts. This is shown in Figure 1.8. A significant amount of the scatter in $i - K$ can be attributed to intrinsic variations in the ultra-violet power-law slopes of the individual quasars, which is why we allow a negative reddening. The SDSS and UKIDSS photometry are separated by $3 - 4$ years in the source rest-frame. Therefore, some of the $i - K$ scatter could be due to temporal variations in the brightness of the targets. However, the red-asymmetry of the $i - K$ colours about the unreddened SED model suggests that this effect is sub-dominant to intrinsic colour differences. However, there is a clear 'red tail' to the colour distribution which can be explained by dust reddening at the redshift of the quasar. We discarded from our sample quasars with $i - K$ colours redder than our standard model with dust reddening $E(B - V) = 0.075$ and bluer than $E(B - V) = -0.075$ (Figure 1.8). Following this cut we are left with 4 615 quasars in our low-z sample and 1 692 quasars in our high-z sample.
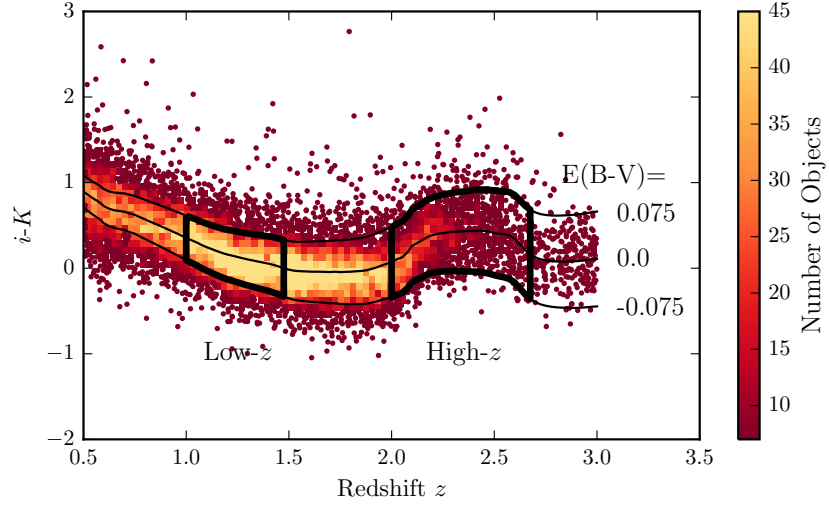
Figure 1.8: $i - K$ colours of non-BALQSO DR7Q quasars with $i > 19.1$ as a function of redshift. The lines show the colours of our model with varying amounts of dust extinction. Quasars with extinction $|E(B - V)| > 0.075$ are excluded.

1.8.3 *Diversity in hot dust properties*

In Figure 1.7 we plot the $W1 - W2$ colours of the sample as a function of redshift at $z < 3$. In this redshift range the $W1$ and $W2$ band-passes are probing the $1.2 - 2.8$ micron and $1.6 - 3.8$ micron region of the rest frame SED respectively. For reference, the peak wavelength is at 2.4 micron for a blackbody radiating at 1200 K. At any given redshift we see a ~ 0.5 mag dispersion in the $W1 - W2$ colours.

On the same axes in Figure 1.7 we have plotted the $W1 - W2$ colours derived from our SED model with a fixed blackbody temperature (1216 K) and a ratio of near-infrared to ultra-violet luminosity ranging from 0.0 to 0.5, with the other model parameters held constant. We conclude that even with the sample restricted to be uniform in its ultra-violet/optical properties, we still get an significant spread in $W1 - W2$ colours, which we can use to learn about the diversity of near-infrared properties in our sample. In the rest of this Chapter we will characterise the hot dust properties of our sample, and test its relation to quasar properties such as luminosity, black-hole mass and normalised accretion rate, and outflow-properties.

We will fit a model to the individual quasar SEDs, allowing the temperature and normalisation of the black body component to vary. The model spectrum is redshifted to the redshift of the quasar being fit and is then multiplied by the ugrizYJHMW1W2W3 throughput functions and normalised appropriately to give AB magnitudes. We minimise the chi-squared statistic using the minimisation is done using the 'nelder-mead' algorithm. To avoid significant absorption in the Lyα forest at high-z, we restrict our fitting to wavelengths greater than 2000 Å; when the effective wavelength of a band-pass falls below this limit the band-pass is excluded from the fit. $W3$ is only used for the quasars at redshifts $2 < z < 2.7$.

2000A is quite large given the Ly-alpha forest impacts from 1216A.

*Show some example fits? Show overlayed data/model with alpha=0.1? e.g. figures/chapter05/ntt_proposal_figure2.pdf*

1.10 RESULTS

In Figure 1.9 we see that the two parameters are clearly correlated. For a lower temperature blackbody the near-infrared to ultra-violet luminosity ratio is larger. Such a correlation is to be expected: as the blackbody temperature is lowered, the peak shifts to longer-wavelengths (following Wien's displacement law). Because of this degeneracy we need to be very careful to separate out real trends of $R_{NIR/UV}$ with other quasar properties from indirect trends resulting from a mutual dependence on T_{BB}.

In Figure 1.9 we show that there is significant range of temperature and normalisation present in our sample. However, we need to quantify how much of this is due simply to uncertainties in the fits stemming from uncertainties in the photometry. In order to achieve this we took our standard SED model with a single temperature and normalisation blackbody component, and generated 200 mock SEDs with a brightness distribution similar to that of our real sample. We estimated the mean uncertainty of the magnitudes in the K, $W1$, and $W2$ band-passes as a function of apparent brightness. We then sampled the K, $W1$, and $W2$ magnitudes from Gaussian distributions, with a mean equal to the magnitude of the model SED, and the width equal to the mean uncertainty at the appropriate brightness. Finally, we fit these mock SEDs using our standard fitting procedure. The results are shown by the red points in Figure 1.9 We can see that scatter introduced by the uncertainty in the photometry is significantly less than the intrinsic scatter in the
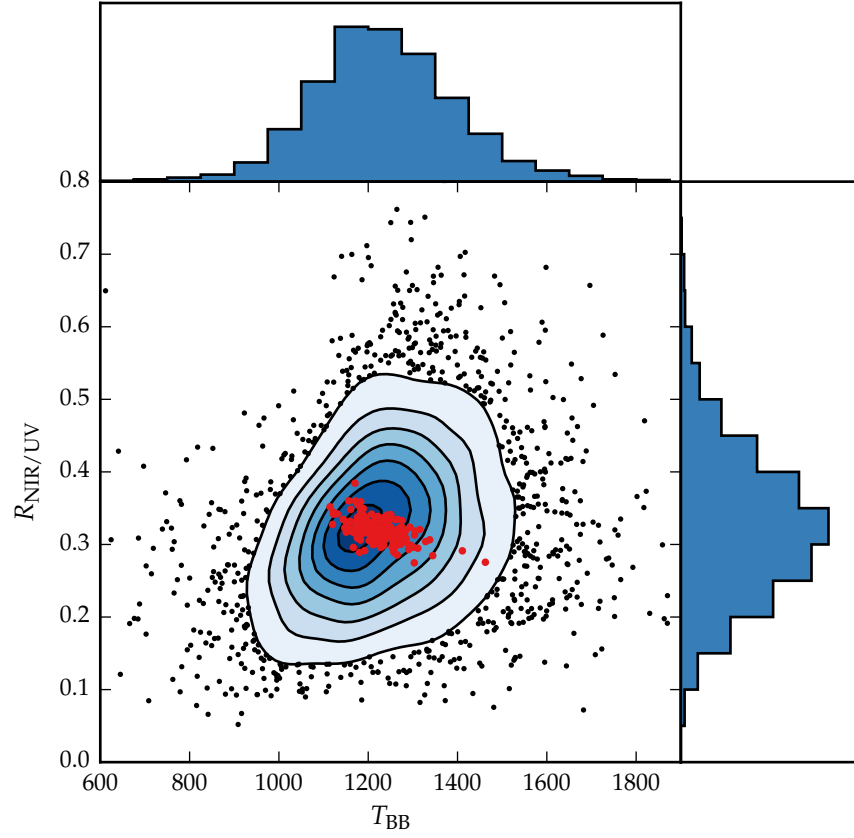
Figure 1.9: Ratio of near-infrared to ultra-violet luminosity ($R_{NIR/UV}$) against temperature (T_{BB}) for low-z sample. The density of points is shown in more dense regions of the space, and individual objects in less dense regions. The red points show the mock data.

data. This demonstrates that there is a real distribution of hot dust temperatures and luminosities in our sample.

1.10.1 *Correlations with quasar properties*

We now look for correlations between the properties of the blackbodies we have fitted to the hot dust emission and other properties of the quasar such as redshift, BH mass, normalised accretion rate (Eddington ratio), and outflow diagnostics.

There is a clear anti-correlation between the ultra-violet luminosity and the best-fit blackbody temperature. We calculated a Spearman rank-order correlation coefficient -0.33. The black-hole masses are virial estimates calculated by Shen et al. 2011 using the MgII emission-line in the SDSS spectra. The Eddington ratios (bolometric luminosity normalised by Eddington luminosity) are also calculated by Shen et al. 2011 using bolometric corrections in Richards et al. (2006a) using 3000Åmonochromatic luminosities. There are no significant correlations between T_BB and $R_{NIR/UV}$ and the ultra-violet luminosity, black-hole mass or Eddington ratio.

The dynamic range in luminosity is very limited. I will combine the low and high z samples. As first step see if there is a difference in the median $R_{NIR/UV}$ for low/high luminosity samples.

At low-z we get a much larger range in blackbody temperatures from our fits. We discussed how the W3 S/N > 5 cut might be be biasing the high-z sample if the subset being removed had properties distinct from the remainder of the sample. The W3 S/N > 5 cut removes about 25 per cent of the sample.

We observe a positive correlation between the black-hole mass and the near-infrared to ultra-violet luminosity ratio which is quite different from what we observed in our low-z sample. We believe that this is just a manifestation of the fact that at high redshift the black-hole masses are derived from CIV. We will show below how the FWHM of CIV has a positive correlation with the hot dust abundance, and large CIV FWHM leads to larger black hole mass estimates. This explains the apparent correlation between the IR/ultra-violet ratio and the black hole mass. Eddington ratio measures the luminosity relative to the Eddington luminosity. Higher BH mass estimates will lead to lower Eddington ratios, which is why the Eddington ratio appears to decrease with increasing IR/ultra-violet ratio. For the sources in our low-z sample the black-hole mass

Calculate new BH masses and redo this section.

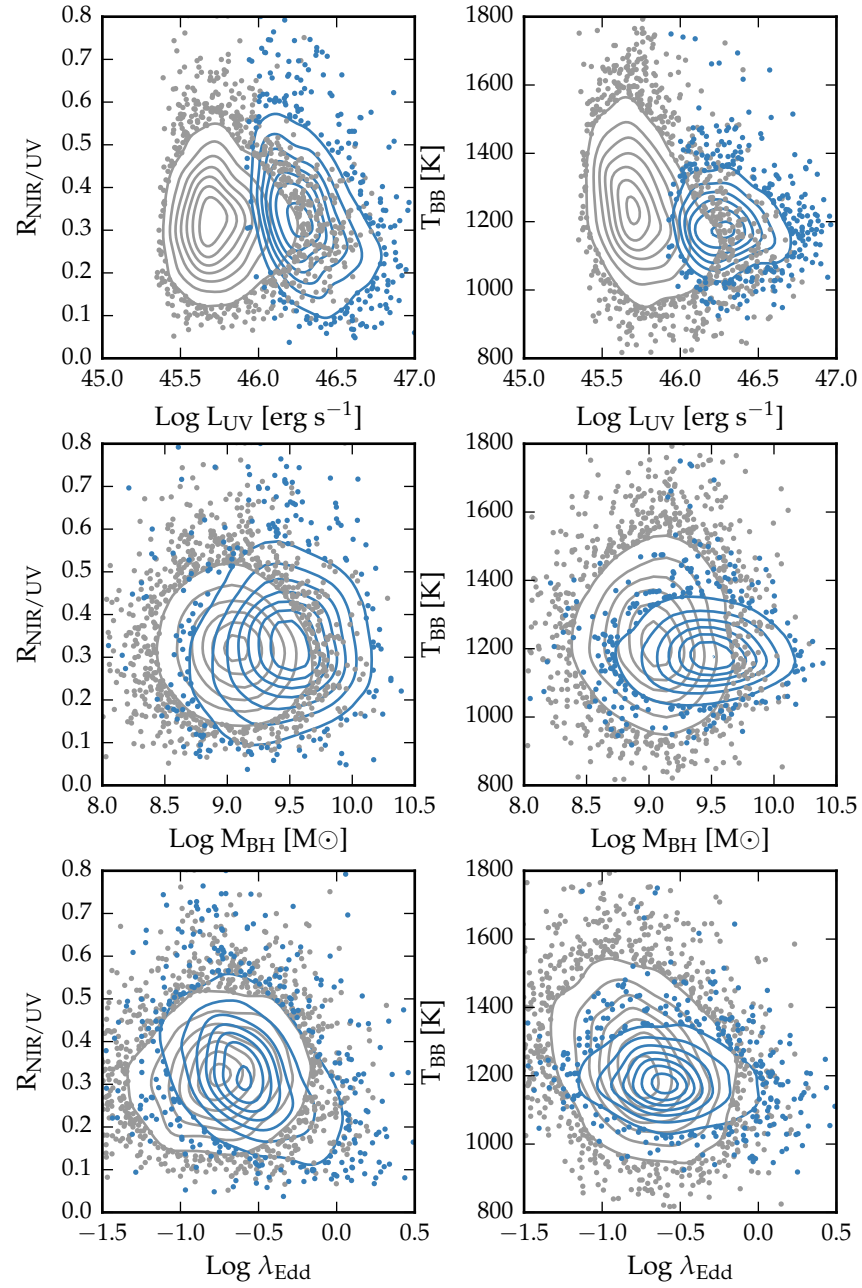*Do we believe this trend is real? This is just for low-z sample.*

Figure 1.10: Best-fit blackbody temperature against ultra-violet luminosity (left), black-hole mass (centre) and Eddington ratio (right) for $1 < z < 1.5$ sample (black) and $2 < z < 2.7$ sample (black). Needs re-making with new BH masses. Maybe just show as one sample?
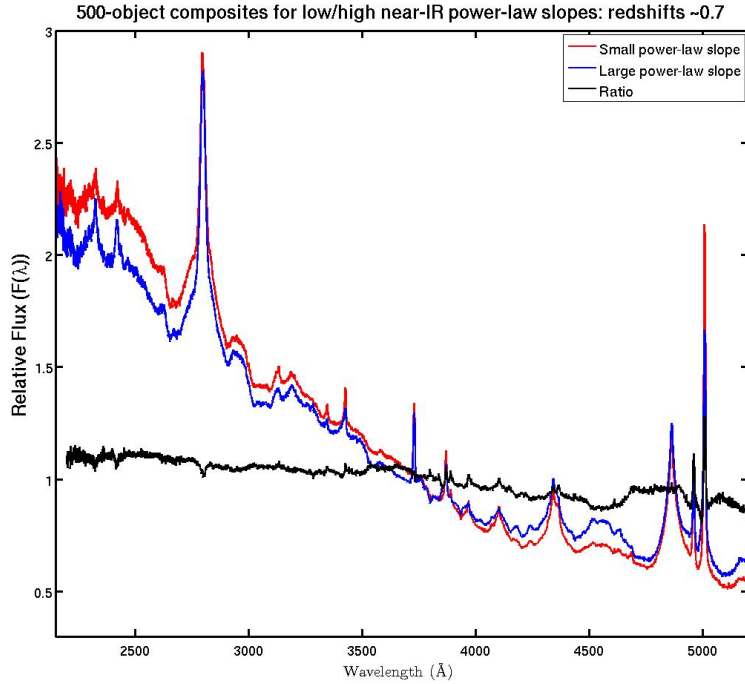
Figure 1.11: Composite SDSS spectra for objects at $z \sim 0.7$. We have divided sample into objects with objects best-fit by small (red line) and large (red line) values of β. Remake if possible.

is measured using the broad MgII emission-line. As we will show below, the properties of the MgII emission-line have no dependence on the hot dust properties.

Composite spectra

Is there a connection between the hot dust properties and EV1? To test this we can divide the quasar sample by hot dust properties, and then generate composite spectra. The EV1 original EV1 correlates - Fe II, Hβ , [O III] - are at around 4000-6000Å. The SDSS spectra are probing shorter wavelengths at redshifts $z \gtrsim 1$. Recall that our sample does not include any quasars at redshifts $z < 1$, where the host galaxy emission starts to become significant.

The $z < 0.8$ SDSS spectrum composite comparison for the small and large β_{NIR} sub-samples (Figure **??**) is a very direct illustration of EV1. Hot dust emission increases with Fe II EW. We also note that the amount of hot dust correlates with the Si III/C III] emission ratios. The Si III/C III] ratio is generally

Need to decide what to do here. If I say host galaxy is significant using the power-law slope won't help. Use blackbody fits instead?

considered to be a good indicator of density and is one of the primary EV1 correlates. The relative flux ratio of Si III to C III] increases when C IV is more blue-shifted (Richards et al., 2011). The Mg II emission-line has exactly the same profile/shape for the two samples (apparent changes in Mg II seen in Figure 1.11 are the result of changes in Fe II at wavelengths just short-ward of the line). Finally, we note that objects with more hot dust are slightly redder.

Shen and Ho, (2014) also find that torus emission is enhanced in quasars with larger R_{FeII}. They suggests that this may be caused by more efficient disc winds that facilitate the formation of a dusty torus.

High-z

In Figure **??** we show how the ratio of near-infrared to ultra-violet luminosity depends on the blueshift and rest-frame EQW of the C IV line. C IV blueshifts are calculated as in Section XX. We see that the near-infrared to ultra-violet luminosity ratio is strongly correlated with the blue-shift of the C IV emission-line. A similar trend was noted by Wang et al., (2013). Interestingly, we note strong similarities to the object subsets selected according to their C IV-emission properties in Richards et al., (2011) (see Figures 11 & 12). We note that the correlation between the hot dust and the C IV emission properties will lead to apparent correlations between the host dust and the BH mass.

1.11 DISCUSSION

Roseboom et al., (2013) studied a similar sample of luminous type 1 quasars. They, like us, modelled the near-infrared emission using a blackbody and modelled the emission at longer wavelengths using a clumpy torus model. They find that while $L_{1-5\mu m}/L_{IR}$ appears relatively insensitive to L_{bol} and L_{IR}, a strong correlation appears between $L_{1-5\mu m}/L_{IR}$ and L_{IR}/L_{bol} (i.e. the dust covering factor). They explain this correlation by postulating that as the covering factor of the torus decreases, the maximum inclination at which a type 1 quasar would be seen increases. An increase in the inclination will mean direct sight lines to more of the inner wall of obscuring material closest to the accretion disc.

Mor and Trakhtenbrot, (2011) also looked at the hot dust properties of a sample of $0.75 < z < 2$ quasars, with photom-
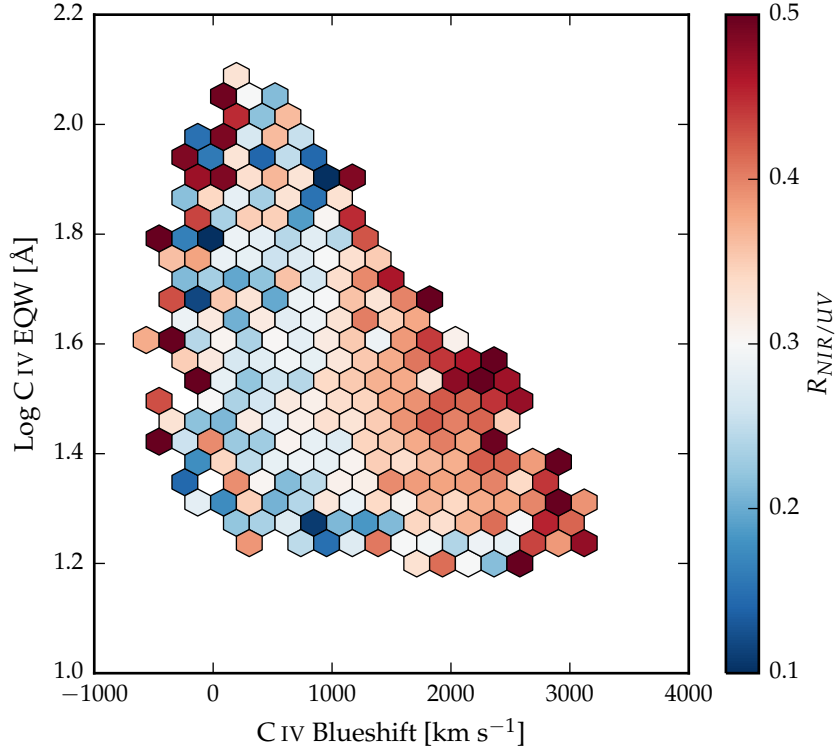
Figure 1.12: Rest-frame EQWand blueshift of the C IV line for 7,115 SDSS DR7 quasars. The colours of the hexagons denote the median hot dust (T≃1200 K) abundance for all quasars at a given EQW and blueshift. Quasars with the most extreme outflow signatures are predominantly hot-dust rich. Only bins containing a minimum of two objects are plotted.
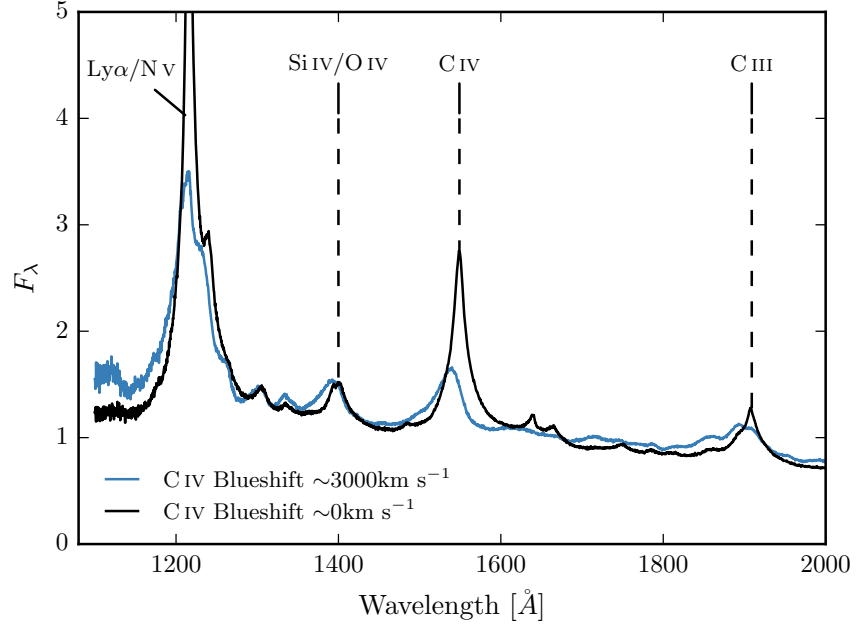
Figure 1.13

etry from SDSS and WISE. They modelled the near-infrared emission with hot clouds of pure graphite dust. They reported an anti-correlation between the covering factor of hot dust clouds and the quasar bolometric luminosity. Like us, they neglect cooler dust components which will dominate the SED at longer wavelengths. As we have discovered (see Figure residual plot), the missing flux decreases with redshift because we observe shorter rest-frame wavelengths when the observed spectrum is redshifted to a greater degree. This will induce an anti-correlation between the luminosity of the hot dust component and the luminosity of the quasar (which is correlated with redshift). At $z = 0.75$, the $W3$ band-pass (the longest in their fits) is sensitive to flux from 6.9 micron; at this wavelength we expect the contribution from cooler dust to dominate over the hot dust. It is possible that this effect could explain the tension with our own result that $R_{NIR/UV}$ does not depend on the quasar luminosity in our low-z sample.

Shen and Ho, (2014) quantify the relative torus emission using the $r - W1$ colour for a sample of $0.4 < z < 0.8$ SDSS quasars. At these redshifts $W1$ is observing between 1.9 and 2.4 micron in the rest-frame of the quasar, which suggests that they are sensitive to the same component of hot dust which we

are investigating. They observe a mild trend of decreasing relative torus emission as the quasar luminosity increases. We note that their use of the $r - W1$ at much higher redshifts may be problematic, as the $W1$ flux will be increasingly dominated by direct emission from the accretion disc.

Gallagher et al., (2007) undertook a similar investigation for a much smaller sample of 234 radio-quiet quasars.

Wang et al., (2013), fitting the near-infrared emission with a single power-law, found that objects with strong outflow signatures (blue-shifted C IV) have more hot dust emission relative to the accretion disc emission in a large sample of $z \sim 2$ non-BAL quasars. Also found by Shen and Ho, (2014).

1.12 DISCUSSION

Ultra-violet photons from the accretion disc accelerate the wind via radiation line driving. Dust absorption contributes to the outflow acceleration. It would be efficiently accelerated by the central continuum source because of the high cross-section of dust (e.g. Fabian, 2012). That flattens the geometry of the wind and exposes more surface area that is viewable on a relatively face-on line of sight. The radiation pressure is increased at higher luminosities and/or accretion rates. This can flatten the geometry of the wind, thereby increasing the range of angles for which the inner edge of the dusty wind - where dust is at it's sublimation temperature - can be observed. A direct prediction is therefore that the in a quasars with high accretion rates and strong outflows, the emission from hot dust should be enhanced. (See Kishimoto picture)